



22 significantly. The influence of earthquake on slope stability is significantly greater than
23 that of rainfall. The corresponding safety factor when the vertical seismic action is
24 vertically downward is smaller than that when it is vertically upward. When considering
25 both horizontal and vertical seismic effects, slope stability is lower.

26 **Keywords**

27 Three-dimensional slopes; Rainfall; Earthquake; Stability analysis

28 **1 Introduction**

29 Landslides often occur due to the combined effects of rainfall and earthquake.
30 Seepage causes an increase in pore water pressure, leading to a decrease in effective
31 stress and shear strength of the soil. The weight of the soil also increases, while seismic
32 inertial forces act unfavorably by accelerating the loss of effective stress. Therefore,
33 these two external forces seriously weaken slope stability. When these two hazards
34 coincide, it often results in computational instability of previously stable slopes. Further
35 research is necessary to investigate the stability of slopes under the combined influence
36 of rainfall and earthquake (David, 2000; Iverson, 2000; Sassa et al., 2010).

37 At present, the main research methods for slope stability include the limit
38 equilibrium method (Bishop, 1955; Morgenstern and Price, 1965; Spencer, 1967), limit
39 analysis (Farzaneh et al., 2008; Michalowski, 1995; Qin and Chian, 2018; Zhou et al.,
40 2017), Finite Element Method (Griffiths and Lane, 1999; Ishii et al., 2012) et al. There
41 have been numerous studies and findings regarding the stability assessment of three-
42 dimensional slopes. However, most of these methods are based on extended three-



43 dimensional equilibrium analysis techniques (Hung, 1987; Zhang, 1988; Chen, 2001;
44 Cheng and Yip, 2007), which rarely strictly adhere to the six equilibrium conditions.
45 Additionally, these approaches often introduce a significant number of assumptions that
46 limit their practical engineering applications. The strict three-dimensional limit
47 equilibrium method proposed by Zheng (2007) is an overall analysis approach based
48 on the natural form of slip surface stress distribution and approximation through shard
49 interpolation. Sun et al. (2016, 2017) combined Morgenstern-Price and Bell global
50 analysis method to analyze the stability of reservoir bank slope, applying this method
51 to the Three Gorges reservoir area. Rahardjo et al. (2010) studied the effect of
52 groundwater table position, rainfall intensities, and soil properties in affecting slope
53 stability using the numerical analyses. Zhou and Qin (2022) proposed a finite element
54 upper bound method for assessing the stability of soil slopes subjected to reservoir
55 water decline and rainfall.

56 As a common geological hazard in seismic zones, earthquake-triggered landslides
57 have been extensively investigated by numerous scholars (Sepúlveda et al., 2005;
58 Chang et al., 2012; Jibson and Harp, 2016; Marc et al., 2017; Salinas-Jasso et al., 2019).
59 At present, the stability analysis method of 3D slope is not mature, and the research on
60 the dynamic stability of 3D slope is even more scarce. The quasi-static method (Liu et
61 al., 2001) introduces coefficients (k_v and k_h) that reflect dynamic action, thereby
62 transforming a dynamic problem into a static one for easier resolution. This approach
63 avoids the complexities associated with dynamic analysis and has become widely used



64 in engineering. Horizontal seismic effects are often a significant consideration in slope
65 stability analysis, however, some research (Chopra, 1966; Lew, 1991; Ling et al., 1999;
66 Shukha and Baker, 2008) confirms that the vertical component of seismic forces should
67 also be given great attention. Wang and Xu (2005) employed the dynamic finite element
68 method to investigate the seismic response characteristics of various components in a
69 three-dimensional high slope, yet failed to determine the safety factor. Guo et al. (2011)
70 obtained the time history curve of slope safety factor during earthquake using vector
71 sum method in two-dimensional situations, but did not extend their findings to three-
72 dimensional situations. Cao et al. (2019) studied the seismic response and dynamic
73 failure mode of the slope subjected to earthquake and rainfall by two model tests, and
74 few studies we have found combining effect of rainfall and earthquake.

75 Most studies only consider the role of a single factor in seepage or earthquake,
76 neglecting the slope stability analysis under combined working conditions. Therefore,
77 analyzing the change law of safety factors for slopes during seepage and seismic action
78 is of great practical value in guiding slope support design and evaluating slope stability.
79 In this paper, a 3D rigorous slice-free method considering seepage and seismic forces
80 to solve the safety factor of bank slopes is proposed. The proposed method strictly
81 satisfies the force balance and moment balance in three directions, without introducing
82 other redundant assumptions.

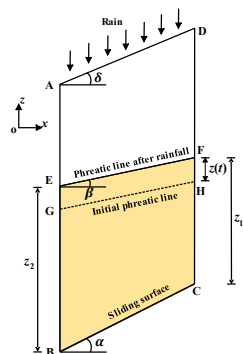


83 **2 Rise of phreatic surface and calculation of seepage force with rainfall**
84 **infiltration in the soil column**

85 A differential soil slice is taken from the slip surface to the slope surface in the
86 landslide body is shown in Fig. 1. $z(t)$ is the rise of phreatic surface after rainfall
87 infiltration, which refers to Conte and Troncone (2017), the height of the soil slice
88 below the phreatic line on BE and CF side are respectively z_1 and z_2 . It is assumed
89 that rainfall is consistent with groundwater movement and that the slope surface is well
90 drained and free of standing water. Regardless of rainfall intensity, runoff will form if
91 it is greater than the infiltration capacity. The height of rise of the phreatic surface within
92 the slope after the rainfall is

93
$$z(t) = \frac{z_r}{n(1-S_r)} \exp\left[-\frac{k}{ds \cos \alpha} i \cos \delta (t-t_0)\right] \quad (1)$$

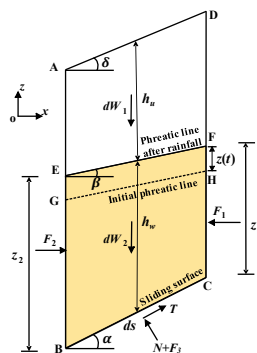
94 where z_r is the volume of water (per unit area) that infiltrates the slope, n is
95 porosity, k is permeability coefficient, S_r is saturation, i is the hydraulic gradient, δ is
96 the angle between the slope surface and the horizontal plane, α is the angle between
97 the sliding surface BC of the differential soil slice and the horizontal plane, ds is the
98 length of the sliding surface BC of the differential soil slice, t is time, and t_0 is the
99 initial moment.



100

101

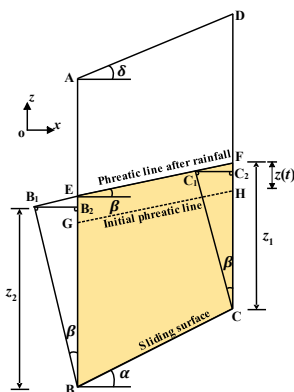
Fig. 1 Relationship between rainfall and groundwater level



102

103

Fig. 2 Calculation sketch of forces acting on the differential soil slice



104

105

Fig. 3 Calculation sketch of hydraulic head



106 The load on the soil slice is shown in Fig. 2. dW_1 and dW_2 are the gravity of the
107 differential soil slice above and below the phreatic line. The resultant hydrostatic force
108 of the boundary AB , CD , and BC are F_1 , F_2 , and F_3 respectively. N is the contact
109 pressure (effective pressure) between the soil particles, and T is the sliding resistance
110 force. β is the angle between the phreatic line and the horizontal plane, h_u and h_w are
111 the height of the soil slice above and below the phreatic line respectively.

112 According to the flow properties of the phreatic line perpendicular to the
113 equipotential line, the surrounding hydrostatic pressures F_1 , F_2 , and F_3 on the
114 boundary CF , BE , and BC can be determined. As shown in Fig. 3, BB_1 and CC_1 are
115 perpendicular to the phreatic line, then make B_1B_2 perpendicular to AB , and C_1C_2
116 perpendicular to CD . According to the geometric relationship, the hydrostatic pressure
117 resultant forces at the boundary CF and BE are

$$118 \quad F_1 = \frac{1}{2} \gamma_w z_1^2 \cos^2 \beta, F_2 = \frac{1}{2} \gamma_w z_2^2 \cos^2 \beta \quad (2)$$

119 γ_w is the unit weight of the water. Let $h_w = \frac{1}{2}(z_1 + z_2)$, the hydrostatic pressure
120 resultant force on the slip surface BC is

$$121 \quad F_3 = \frac{1}{2} \gamma_w (z_1 + z_2) d s \cos^2 \beta = \gamma_w h_w d s \cos^2 \beta \quad (3)$$

122 The components of F_3 in the horizontal and vertical directions are

$$123 \quad U_x = \gamma_w h_w d s \cos^2 \beta \cos \alpha, \quad U_y = \gamma_w h_w d s \cos^2 \beta \sin \alpha \quad (4)$$

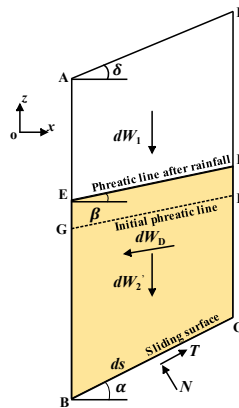
124 The gravity of water in differential soil slice is

$$125 \quad dW_{2w} = \gamma_w h_w d s \cos \alpha \quad (5)$$

126 The permeability pressure is a pair of balancing forces with the water weight in a



127 differential soil slice and the hydrostatic pressure around it (Zheng et al., 2004).
 128 Therefore, the weight of water in the differential soil slice and the surrounding
 129 hydrostatic pressure can be replaced by a seepage force. The force diagram in Fig. 2
 130 can be replaced by Fig. 4. dW'_2 represents the effective unit weight of the soil below
 131 the phreatic line and dW_D is the seepage force.



132
 133 **Fig. 4** Simplified force diagram on a differential soil slice

134 The horizontal and vertical component of the seepage force dW_3 are

135
$$dW_{Dx} = F_1 - F_2 + U_x = \gamma_w h_w \cos^2 \beta (z_1 - z_2 + dss \sin \alpha) \quad (6)$$

136
$$dW_{Dy} = dW_{2w} - U_y = \gamma_w h_w dscos \alpha \sin^2 \beta \quad (7)$$

137 According to geometric relation

138
$$z_1 - z_2 + dss \sin \alpha = dscos \alpha \tan \beta \quad (8)$$

139 Therefore, the seepage force is

140
$$dW_D = \gamma_w h_w dscos \alpha \sin \beta \quad (9)$$

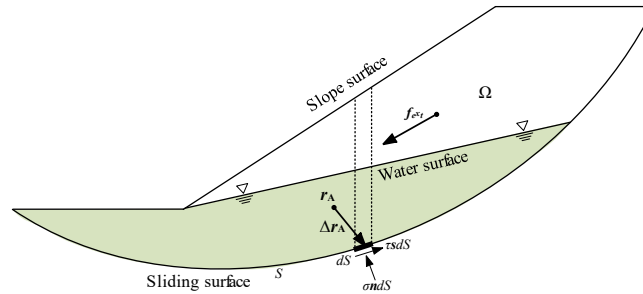
141 The direction of seepage force is consistent with water flow.



142 **3 A global analysis method for slope stability under seepage and**
 143 **earthquake**

144 **3.1 Overall system of equilibrium equations**

145 As shown in Fig. 5, taking the whole sliding body Ω as the research object, and
 146 S is a potential slip surface.



147

148 **Fig. 5** A 2D schematic plot for force system in/on the sliding body

149 dS is a differential element on the sliding surface S . The normal force on a
 150 differential element dS at point \mathbf{r} is $\sigma n dS$, the resultant shear force is $\tau s dS$, \mathbf{n}
 151 (specified pointing to the inside of the slide Ω) is the unit normal vector at position
 152 vector \mathbf{r} , and \mathbf{s} (specified opposite to the sliding direction) is the unit tangent vector,
 153 so the reaction on dS is:

154
$$d\mathbf{f} = (\sigma \mathbf{n} + \tau \mathbf{s}) dS \quad (10)$$

155
$$d\mathbf{m}_A = \Delta \mathbf{r}_A \times d\mathbf{f} \quad (11)$$

156 Here, $\Delta \mathbf{r}_A = \mathbf{r} - \mathbf{r}_A$, \mathbf{r} is the position vector of dS , \mathbf{r}_A is the position vector for any
 157 given reference point A , “ \times ” represents vector multiplication.

158 \mathbf{f}_{ext} is the resultant external force vector, including external loads such as gravity,
 159 seepage force, seismic force et al.; \mathbf{m}_{ext} denotes the moment \mathbf{f}_{ext} concerning \mathbf{r}_A . To



160 integrate over the entire sliding surface dS :

$$161 \quad \iint_S d\mathbf{f} + \mathbf{f}_{ext} = \mathbf{0} \quad (12)$$

$$162 \quad \iint_S d\mathbf{m}_A + \mathbf{m}_{ext} = \mathbf{0} \quad (13)$$

163 According to Mohr-Coulomb criterion,

$$164 \quad \tau = \frac{1}{F_s} [c' + f'(\sigma - u)] = \frac{1}{F_s} (c_w + f'\sigma) \quad (14)$$

165 Here, F_s is the safety factor, c' and f' are the effective stress shear strength
 166 parameters, u is the pore pressure; c_w is defined as

$$167 \quad c_w \equiv c' - f'u \quad (15)$$

168 Order,

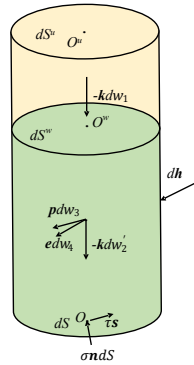
$$169 \quad \mathbf{n}' = \begin{pmatrix} \mathbf{n} \\ \Delta\mathbf{r}_A \times \mathbf{n} \end{pmatrix}, \quad \mathbf{s}' = \begin{pmatrix} \mathbf{s} \\ \Delta\mathbf{r}_A \times \mathbf{s} \end{pmatrix}, \quad \mathbf{f}_m = \begin{pmatrix} \mathbf{f}_{ext} \\ \mathbf{m}_{ext} \end{pmatrix} \quad (16)$$

170 Substituting equations (10), (11), and (14) into equations (12) and (13), and
 171 merging into a more compact form:

$$172 \quad F_s \left(\iint_S \mathbf{n}' \sigma dS + \mathbf{f}_m \right) + \iint_S (c_w + f'\sigma) \mathbf{s}' dS = \mathbf{0} \quad (17)$$

173 3.2 Normal stress expression of slip surface under seepage force and seismic force

174 As shown with the dash line in Fig. 5, a vertical differential cylinder is now taken
 175 from the homogeneous sliding body from the slip surface to the slope surface. The load
 176 on the differential cylinder is shown in Fig. 6. $-kdw_1$ is the weight of the soil above
 177 phreatic surface, and $-kdw'_2$ refer to the floating weight of the soil below the phreatic
 178 surface. pdw_3 and edw_4 denote the seepage force and seismic force. $d\mathbf{h}$ refers to the
 179 action force of the soil around the differential cylinder.



180

181 **Fig. 6** Sketch of force acting on a vertical differential cylinder in a sliding body

182 Here, \mathbf{k} = unit vector of z -axis; \mathbf{p} = unit vector pointing to the direction of the
 183 seepage force; \mathbf{e} = unit vector pointing to the direction of the seismic force; θ = angle
 184 between dS and the horizontal plane; ξ = angle between the phreatic surface dS^w and
 185 the horizontal plane in the differential cylinder.

186 The force equilibrium condition for a differential cylinder is

$$187 \quad \sigma ndS + \tau_s dS - kdw_1 - kdw_2 + pdw_3 + edw_4 + dh = \mathbf{0} \quad (18)$$

188 Both sides of the Eq. (18) are simultaneously multiplied by \mathbf{n} to obtain

$$189 \quad \sigma = n_3 \left(\frac{dw_1}{dS} + \frac{dw_1'}{dS} \right) - n_p \frac{dw_3}{dS} - n_e \frac{dw_4}{dS} - \frac{\mathbf{n} \cdot d\mathbf{h}}{dS} \quad (19)$$

190 Here, n_3 = component of \mathbf{n} in the positive direction of z -axis, n_p = projection of
 191 \mathbf{p} in \mathbf{n} direction, n_e = projection of \mathbf{e} in \mathbf{n} direction.

192 Known,



$$\begin{cases}
 dw_1 = \bar{\gamma} H_u dS \cos \theta \\
 dw_2 = \bar{\gamma}' H_w dS \cos \theta \\
 dw_3 = \gamma_w H_w dS \cos \theta \sin \xi \\
 dw_4 = k_c (\bar{\gamma} H_u + \bar{\gamma}_{sat} H_w) dS \cos \theta \\
 n_p = \mathbf{n} \cdot \mathbf{p} \\
 n_e = \mathbf{n} \cdot \mathbf{e}
 \end{cases} \quad (20)$$

194 where, $\bar{\gamma}$ = average value of the unit weight of the soil above the phreatic surface; $\bar{\gamma}'$
 195 = average value for the unit floating weight of the soil below the phreatic surface; $\bar{\gamma}_{sat}$
 196 = average value of the unit saturated weight of below the phreatic surface; γ_w = unit
 197 weight of water; H_u = height of soil above the phreatic surface; H_w = height of the soil
 198 below the phreatic surface; k_c = seismic force coefficient.

199 Substitute Eq. (20) into Eq. (19) and sort it out

$$\sigma = (\gamma H_u + \gamma' H_w) \cos^2 \theta - n_p \gamma_w H_w \cos \theta \sin \xi - n_e k_c (\gamma H_u + \gamma_{sat} H_w) \cos \theta - \frac{\mathbf{n} \cdot d\mathbf{h}}{dS} \quad (21)$$

201 Order

$$\begin{aligned}
 \sigma_0 &= (\gamma H_u + \gamma' H_w) \cos^2 \theta - n_p \gamma_w H_w \cos \theta \sin \xi - n_e k_c (\gamma H_u + \gamma_{sat} H_w) \cos \theta, \\
 h_n &= -\frac{\mathbf{n} \cdot d\mathbf{h}}{dS}
 \end{aligned} \quad (22)$$

203 Therefore

$$\sigma = \sigma_0 + h_n \quad (23)$$

205 Here, σ_0 = contribution of volume force to the normal stress. h_n = contribution
 206 of the force of surrounding soil to the normal stress of sliding surface.

207 The normal stress distribution of the slip surface can be approximated in the
 208 following (Zheng, 2009):

$$\sigma = \sigma_0 + f(x, y; \mathbf{a}) \quad (24)$$

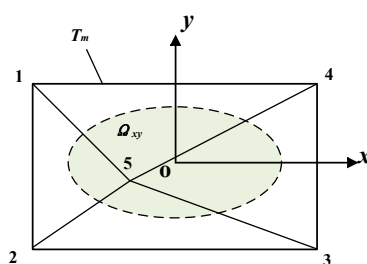
210 where $f(x, y; \mathbf{a})$ = function in the horizontal coordinates (x, y) with a parametric



211 vector \mathbf{a} consisting of five unknowns. $f(x, y; \mathbf{a})$ is constructed by piecewise triangular
 212 linear interpolation:

$$213 \quad f(x, y; \mathbf{a}) = \mathbf{l} \mathbf{a} \quad (25)$$

214 where \mathbf{l} is the interpolation function, $\mathbf{l} = (l_1, l_2, \dots, l_5)$, and it satisfies $\sum_{i=1}^5 l_i = 1$.



215

216 **Fig. 7** A triangular mesh for interpolation of normal stress on slip surface

217 As shown in Fig. 7, Ω_{xy} is the projection of the sliding body on the xoy plane, the
 218 area characterized by the dashed line. T_m is a triangular network containing 5 nodes.
 219 $l_i(x, y) (i = 1, 2, \dots, 5)$ is the interpolation function for these 5 nodes, which can be
 220 formed as in finite elements with the help of the area coordinates of the 4 triangles on
 221 T_m .

222 Substitute Eq. (24) into Eq. (17), a system of nonlinear equations with F_s and \mathbf{a} as
 223 unknowns is obtained:

$$224 \quad F_s \mathbf{B} \mathbf{a} + \mathbf{D} \mathbf{a} + F_s \mathbf{b} + \mathbf{d} = 0 \quad (26)$$

225 Where \mathbf{B} and \mathbf{D} are both matrices of order 6×5 , and \mathbf{b} and \mathbf{d} are both vectors of
 226 order six, whose expressions are respectively



$$\left\{ \begin{array}{l} \mathbf{B} = \iint_s \mathbf{n}' t dS \\ \mathbf{D} = \iint_s f' s' t dS \\ \mathbf{b} = \mathbf{f}_m + \iint_s \sigma_0 \mathbf{n}' dS \\ \mathbf{d} = \iint_s (c_w + f' \sigma_0) s' dS \end{array} \right. \quad (27)$$

228 We can solve Eq. (26) by either Newton's method or eigenvalue method.

229 In Eq. (26), all terms except the resultant external force (moment) \mathbf{f}_m are area
230 integrals. The volume integrals on the sliding body involved in the problem are
231 transformed into boundary integrals that can skip the column partitions. Hence, it is not
232 required to divide the sliding body into columns anymore, only the surface of the sliding
233 body needs to be partitioned, as detailed in Zheng (2007).

234 4 Verification examples

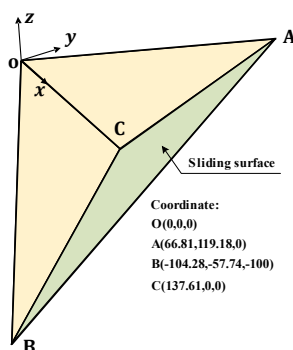
235 In order to verify the accuracy of the proposed method, two examples are analyzed
236 in this section. Different working conditions were set up for Example 2 and the results
237 are compared with those calculated by the software.

238 4.1 Example 1: translational sliding

239 Wedge stability in rock mechanics is a typical 3D limit equilibrium analysis
240 problem. Examples of wedge include two cases of geometric symmetry and asymmetry.
241 Example 1 is an asymmetric wedge. Fig. 8 shows the three-dimensional model and
242 geometric parameters of the wedge plane sliding. The sliding surface is composed of
243 two structural planes, ABC and OAB, and the left and right structural planes of the
244 wedge adopt the same shear strength: $c' = 50\text{kPa}$ and $\varphi' = 30^\circ$. The unit weight of the
245 wedge is 26 kN/m^3 . For simple wedges, the 3D limit equilibrium method has analytical



246 solutions, but these methods all include an assumption that the shear force on the bottom
247 slip plane is parallel to the intersecting prism. If the sliding direction of the wedge
248 sliding body is assumed to be parallel to the intersection line AB of the two structural
249 planes, the wedge sliding body is statically determinate, and the safety factor has an
250 exact value of 1.640 (Hoek and Bray, 1977) for this example. The safety factor
251 calculated based on the method in this paper is 1.652. It demonstrates that the proposed
252 method can reasonably evaluate the stability of rocky slopes containing different
253 structural surfaces.



254

255 **Fig. 8** Model and geometric parameters of the wedge

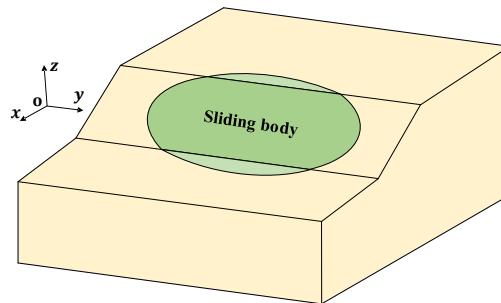
256 **4.2 Example 2: ellipsoidal sliding**

257 In order to verify the feasibility of the proposed method for calculating the slope
258 stability under seepage and earthquake, a classical ellipsoid example is selected for the
259 stability analysis, which is derived from the study of Zhang (1988). Zhang's (1988)
260 paper in 1988 provides a three-dimensional slope ellipsoid slip surface example, and
261 the simplified three-dimensional limit equilibrium method (only three force equilibrium
262 and one moment equilibrium are satisfied) is used for the stability analysis. Zhang's



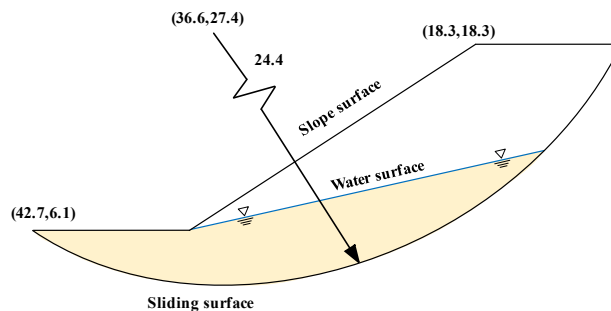
263 (1988) solution for the 3D limit equilibrium of a symmetric ellipsoid can be regarded
 264 as a rigorous solution since the ellipsoid has a symmetric sliding surface and the other
 265 two moment equilibrium conditions are automatically satisfied by the symmetric bar-
 266 column method. Zhang's (1988) solution has also been used by many scholars to check
 267 the correctness of their own procedures. The example is a homogeneous slope, the
 268 potential sliding surface is a part of a simple ellipsoid, the sliding surface is symmetric
 269 about the xoz plane, and the equation of the sliding surface is

$$270 \quad \left(\frac{x-36.6}{24.4}\right)^2 + \left(\frac{y}{66.9}\right)^2 + \left(\frac{z-27.4}{24.4}\right)^2 = 1 \quad (26)$$



271
 272

Fig. 9 Model of ellipsoid example



273
 274

Fig. 10 Geometric parameters and middle profile with groundwater

275 The ellipsoid model is shown in Fig. 9. The external load of the slope is only



276 considered the effect of gravity, the unit gravity is 19.2kN/m^3 , and the effective shear
277 strength parameter: $c' = 29.3\text{kPa}$ and $\phi' = 20^\circ$. Four working conditions are
278 considered in this section, case-1: no groundwater is considered as in the computational
279 model of Zhang (1988); case-2: groundwater is set up as shown in Fig. 10; case-3:
280 earthquake action in the horizontal direction is considered; case-4: both groundwater
281 and horizontal earthquake action are considered. The earthquake acceleration is $0.05g$
282 and the horizontal earthquake direction is taken as along the x-axis positive direction.

283 Case-1: The safety factor calculated using our proposed method is 2.054, whereas
284 Zhang (1988) obtained a result of 2.122 using the limit equilibrium method.
285 Additionally, we perform a 2D stability analysis of the intermediate cross-section of the
286 model using Rocscience's Slide software, and obtain a safety factor of 2.084.
287 Comparing the results mentioned above, it becomes evident that our proposed method
288 for slope stability analysis is feasible, and its calculation results are consistent with the
289 results obtained by using the traditional limit equilibrium method and two-dimensional
290 stability analysis.

291 Case-2: Only the effect of groundwater seepage is considered, and the
292 groundwater not only induces hydrodynamic effects, but also softens the geotechnical
293 materials, leading to a significant decrease in the strength of the soil. In this working
294 condition, the calculated safety factor is 1.183, which is close to 1.057 calculated by
295 Rocscience's Slide.

296 Case-3: We only consider the effect of horizontal earthquake on slope stability. In



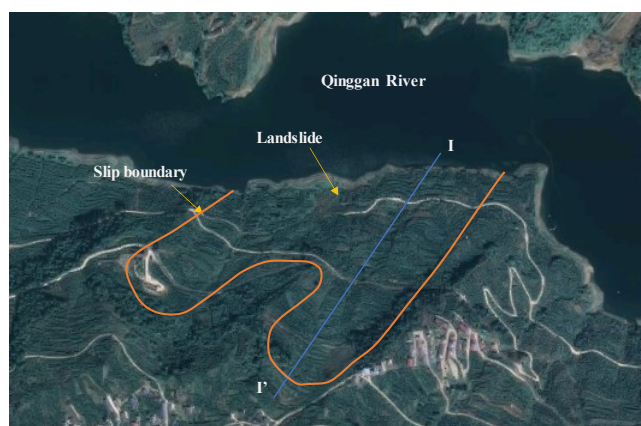
297 order to compare the results with the 2D stability calculations, we choose the horizontal
298 seismic action direction to be in the xoz plane. The results calculated by the 3D
299 procedure and the 2D software are 1.855 and 1.861, respectively. Compared with the
300 case-2, the effect of seepage on the slope stability is greater than that of seismic action.

301 Case-4: We considered both seepage and horizontal seismic effects. In this case,
302 the results calculated by 3D program and 2D software are 1.047 and 0.934 respectively.

303 Based on the above calculation results, we can conclude that the proposed method
304 shows reliability in calculating the slope stability under seepage and seismic actions.
305 The calculation results under different working conditions reinforce this conclusion.

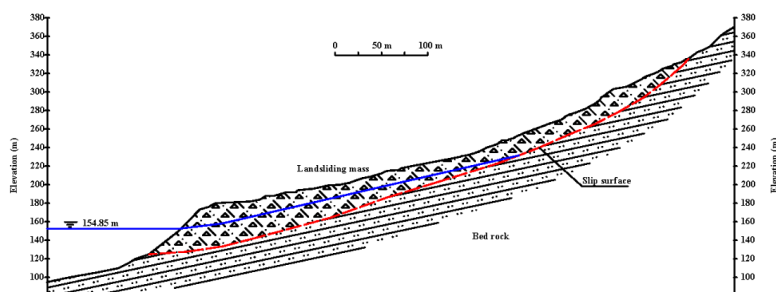
306 5 A True 3D Slope

307 This section investigates slope stability evolution under the influence of rainfall
308 and earthquake by taking an actual slope in the Three Gorges reservoir as a case study.



309

310 **Fig. 11** Geographical location map of Woshaxi slope (© Google Maps)



311

312

Fig. 12 Geological section map of Woshaxi slope

313

314

315

316

317

318

319

320

321

322

323

324

325

326

327

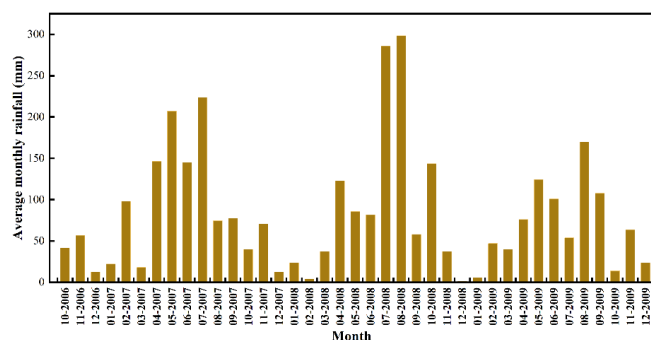
328

The geographical location of the Woshaxi landslide is depicted in Fig. 11, while the cross-section of the landslide (I-I') is illustrated in Fig. 12. Situated on the right bank of Qinggan River, a tributary of Yangtze River, and approximately 1.5km away from Qianjiangping landslide on its left bank. The landslide has been affected by water level fluctuations ranging between 145-175m that have submerged its frontal edge by up to 20-50m. The Woshaxi landslide exhibits a high-to-low gradient from southwest to northeast, with its rear edge situated at an elevation of 405m and the front edge below 140m. This geological event boasts an average thickness of approximately 15m and a volume of $4.2 \times 10^6 \text{ m}^3$, while its primary sliding direction is oriented at 40° .

According to the Seismic Ground Motion Parameter Zonation Map of China, the peak ground motion acceleration in this region is 0.05g. To investigate slope stability evolution under seismic conditions, peak accelerations are calculated and analyzed at various levels. The most dangerous case is considered in the following calculations, where the direction of the horizontal seismic action coincides with the primary sliding direction. The precipitation pattern in this region is characterized by relatively concentrated temporal and spatial distribution. Most of the rainfall occurs between



329 April and October. To investigate the stability of three-dimensional slopes under the
 330 combined influence of rainfall and earthquake, this study considers the effects of three
 331 geotechnical parameters: permeability coefficient, porosity, and saturation. The
 332 proposed method is applied to calculate changes in slope stability resulting from
 333 average monthly rainfall and earthquake occurring between 2007-2009.



334

Fig. 13 Average monthly rainfall from 2007 to 2009

335

336 Fig. 13 shows the average monthly rainfall from 2007 to 2009. Table 1 lists the
 337 physical and mechanical parameters of the landslide body. It is assumed that the
 338 reservoir water level remains unchanged. To assess the effects of different geotechnical
 339 parameters and seismic action on the safety factor, four cases are considered: (i) rainfall
 340 only, (ii) rainfall and horizontal earthquake, (iii) rainfall and vertical earthquake, and
 341 (iv) rainfall and earthquake in both horizontal and vertical directions.

342

Table 1 Mechanical parameters of Woshaxi slope

Unit weight, γ (KN/m ³)		Shear strength, c' (kPa)		Friction angle, ϕ' (°)	
Saturated condition	Natural condition	Saturated condition	Natural condition	Saturated condition	Natural condition
22.4	20.8	18	22	10	20



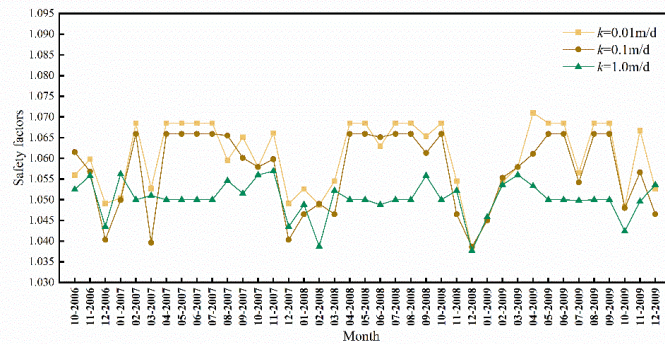
343 (i) Rainfall only

344 The three parameters, infiltration coefficient, porosity, and saturation, have
345 different effects on the safety factor of slopes. The safety factor varies with the monthly
346 rainfall. The analysis shows that an increase in rainfall does not necessarily lead to a
347 lower safety factor. This is because the increase in rainfall leads to a higher phreatic
348 surface, which causes changes in two aspects: an increase in hydrodynamic and an
349 increase in pressure at the foot of the slope. When the pressure at the foot of the slope
350 has more influence on the slope than the hydrodynamic, the safety factor will increase
351 at this time, and conversely the stability of the slope will decrease. As shown in Fig.
352 14(a), the permeability coefficient k is 0.01, 0.1 and 1m/d, respectively. With other
353 parameters unchanged, the trend of safety factor variation for Woshaxi landslide is
354 consistent. The higher the permeability coefficient, the greater the soil's ability to allow
355 water to pass through above the phreatic surface, the smaller the rise of the phreatic
356 surface within the slope. This results in a smaller increase in pressure at the foot of the
357 slope and a lower safety factor.

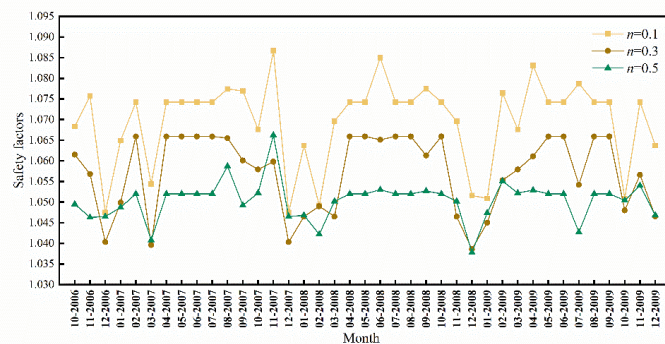
358 As shown in Fig. 14(b), the porosity n is 0.1, 0.3 and 0.5, respectively, and the
359 safety coefficient of the Woshaxi landslide is consistent under the condition that other
360 parameters remain unchanged. The higher the porosity, the greater the soil permeability
361 above the phreatic surface, the smaller the rise of the phreatic surface within the slope,
362 resulting in a smaller increase of pressure at the slope's foot and thus a lower safety
363 factor.



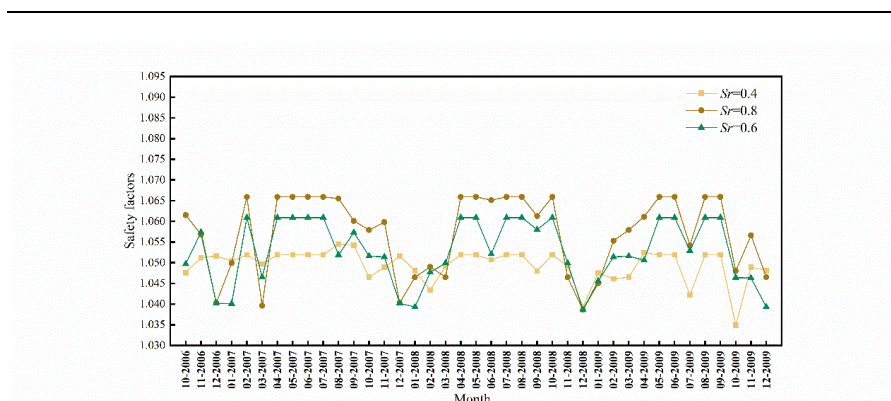
364 As shown in Fig. 14(c), the saturation S_r of the soil above the phreatic surface of
365 the landslide is 0.4, 0.6 and 0.8, respectively, and the safety factor of the Woshaxi
366 landslide is consistent under other parameters remained unchanged. The higher the
367 saturation, the lower the permeability of soil above the phreatic surface, resulting in a
368 greater rise of phreatic surface within the slope and an increased pressure at its foot,
369 thereby leading to a higher safety factor. Overall, under rainfall conditions, soil porosity
370 on the phreatic surface has a greater impact on safety factor than permeability
371 coefficient and saturation.



372
373 (a) permeability coefficient



374
375 (b) porosity



376

377

(c) saturation

378

Fig. 14 Safety factors of the Woshaxi landslide under rainfall

379

(ii) Rainfall and horizontal earthquake

380

Fig. 15 shows the evolution of the stability of the Woshaxi landslide under the

381

combined effect of rainfall and horizontal earthquake with different geotechnical

382

parameters, and the horizontal earthquake coefficient k_h is taken as 0.05. Comparing

383

with Fig. 14, it can be observed that after considering the effect of horizontal earthquake,

384

the variation trend of the safety factor of the Woshaxi landslide calculated with different

385

geotechnical parameters is consistent with that under the rainfall condition only, but the

386

stability of the landslide is obviously decreased. Fig. 16 shows the evolution of the

387

stability of the Woshaxi landslide with rainfall and different horizontal earthquake

388

coefficients. With other parameters unchanged, the values of the horizontal earthquake

389

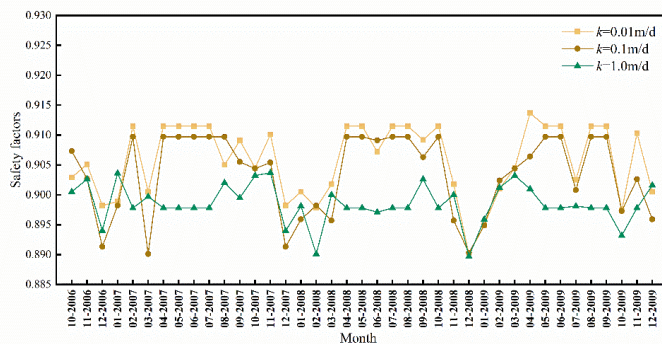
coefficients are 0.05, 0.1 and 0.15 respectively. As the horizontal earthquake coefficient

390

increases, the safety factor of the landslide decreases significantly. The seismic

391

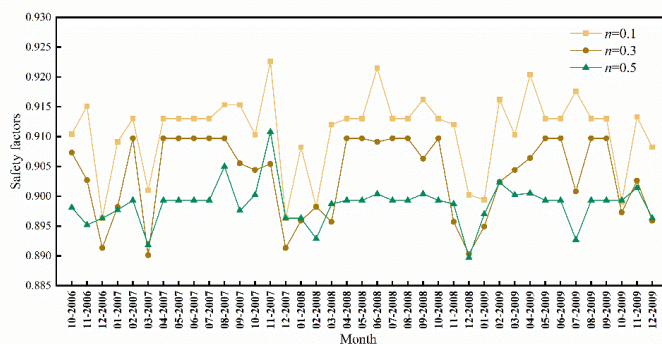
influence on slope stability is considerably greater than that of rainfall.



392

393

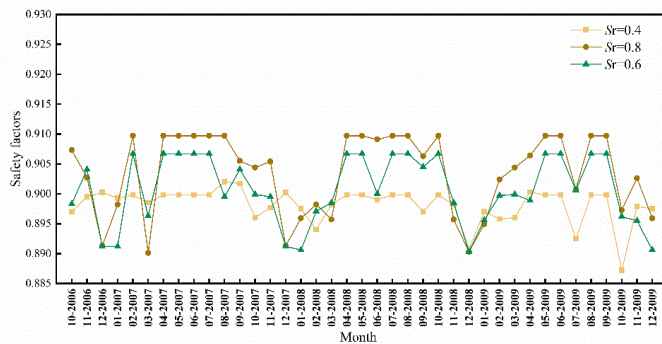
(a) permeability coefficient



394

395

(b) porosity



396

397

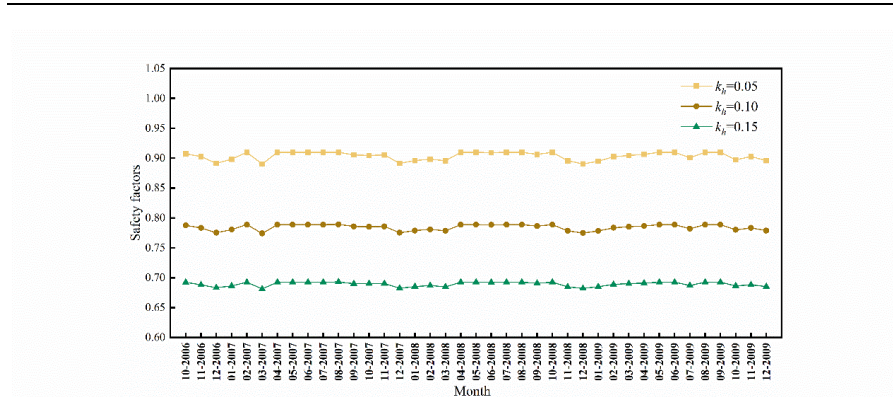
(c) saturation

398

Fig. 15 Safety factors of the Woshaxi landslide under rainfall and horizontal

399

earthquake ($k_h = 0.05$)

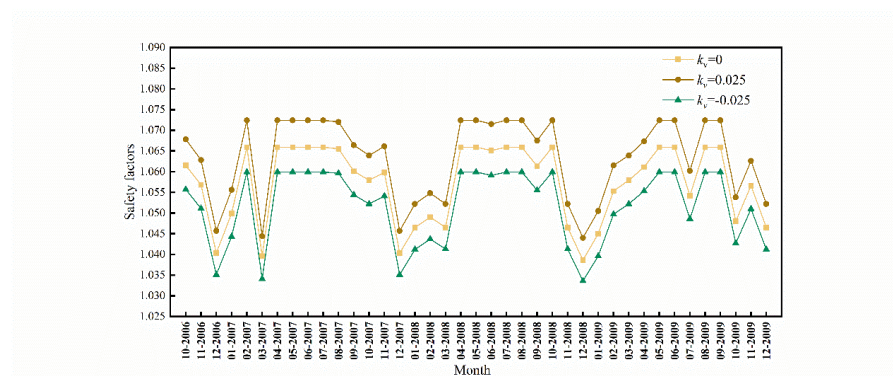


400

401 **Fig. 16** Safety factors of the Woshaxi landslide under rainfall and horizontal
 402 earthquake (different horizontal seismic coefficient)

403 (iii) Rainfall and vertical earthquake

404 Fig. 17 shows the evolution of the stability of the Woshaxi landslide with rainfall
 405 and different vertical earthquake coefficients. With other parameters unchanged, the
 406 vertical earthquake coefficient k_v takes on values of 0.025, 0, and -0.025 respectively,
 407 and the negative sign indicates that the direction of vertical earthquake is vertically
 408 downward. It is obvious from Fig. 17 that the corresponding safety factor when the
 409 earthquake acts vertically downward is smaller than the corresponding safety factor
 410 when it is vertically upward.

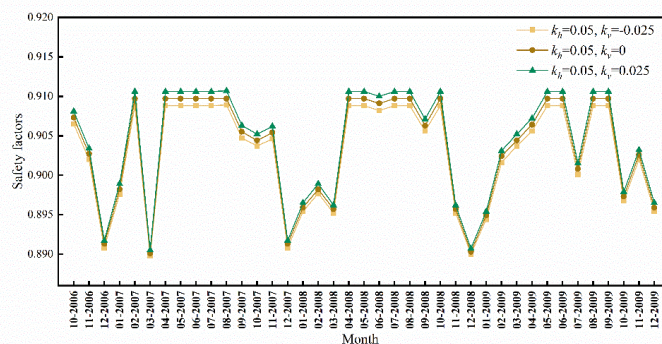


411



412 **Fig. 17** Safety factors of the Woshaxi landslide under rainfall and vertical earthquake
413 (iv) Rainfall and earthquake in both horizontal and vertical directions

414 Fig. 18 shows the evolution of the stability of the Woshaxi landslide with rainfall
415 and different earthquake coefficients. Horizontal earthquake coefficient k_h is taken as
416 0.05, and the values of vertical earthquake coefficient are 0.025, 0, -0.025 respectively,
417 and the negative sign indicates that the direction of vertical earthquake action is
418 vertically downward. Under the condition that other parameters remain unchanged, the
419 slope stability is lower when considering both horizontal and vertical upward
420 earthquake compared to considering only horizontal earthquake. Therefore, it is
421 essential to properly account for the effect of vertical earthquake in order to ensure
422 maximum safety.



423
424 **Fig. 18** Safety factors of the Woshaxi landslide under rainfall and earthquake (in both
425 horizontal and vertical directions)

426 6 Conclusions

427 In this paper, the calculation of the seepage force is studied, the normal stress
428 expression on the sliding surface of a slope under seepage force and seismic force are



429 also derived. Furthermore, a global analysis method that considers both seepage and
430 seismic forces is proposed to determine the safety factor of slopes subjected to the
431 combined effect of rainfall and earthquake. The reliability of the proposed method is
432 also verified with two examples combining software calculations and previous results.

433 Taking a slope in the Three Gorges reservoir area as an example, this study
434 investigates the influence of soil permeability coefficient, porosity and saturation on
435 slope stability, and analyzes the safety evolution of this slope under combined effects
436 of rainfall and earthquake. The results indicate that, under rainfall conditions, the
437 porosity of the soil above the phreatic surface exerts a greater influence on safety factor
438 than permeability coefficient and saturation. With an increase in the horizontal
439 earthquake coefficient, the safety factor of the landslide is significantly reduced, and
440 the impact of earthquake on slope stability surpasses that of rainfall. The safety factor
441 corresponding to vertical downward earthquake action is smaller than that of vertical
442 upward, and the stability of slope is lower when considering horizontal and vertical
443 upward earthquake actions. Therefore, in order to ensure maximum safety, proper
444 consideration should be given to vertical earthquake actions.

445 Considering the effect of seismic force and seepage force, the formula for
446 calculating the stability of landslide under the combined effect of earthquake and
447 rainfall is improved, and the stability coefficient of the landslide is calculated to be low
448 and unstable. The research results provide scientific basis for slope stability analysis
449 and prevention. Further, the proposed method can identify potential risk areas for



450 landslide hazards, and planners in the Three Gorges Reservoir area can better consider
451 these risks and take measures to increase the seismic and flood resilience of reservoir
452 infrastructure.

453 **Data availability**

454 The data used in this study are available from the first author upon request.

455 **Author contribution**

456 JW analyzed the data, conceived the paper, and wrote the paper; ZW conceived
457 and co-wrote the paper; HL reviewed and improved the analysis and paper; and GS
458 provided the data of the actual slope in the Three Gorges reservoir.

459 **Competing interests**

460 The contact author has declared that none of the authors has any competing
461 interests.

462 **Acknowledgments**

463 This study was supported by the National Natural Science Foundation of China
464 (Grant No.11972043).

465 **References**

- 466 Bishop, A.W. 1955. The use of the slip circle in the stability analysis of slopes.
467 *Geotechnique* 5 (1): 7-17.
- 468 Cao, L.C., Zhang, J.J., Wang, Z.J., Liu, F.C., Liu, Y., Zhou, Y.Y. 2019. Dynamic
469 response and dynamic failure mode of the slope subjected to earthquake and rainfall.
470 *Landslides* 16, 1467-1482. <https://doi.org/10.1007/s10346-019-01179-7>.



-
- 471 Chang, K.T., Lin, M.L., Dong, J.J., Chien, C.H. 2012. The hungtsaiping landslides:
472 from ancient to recent. *Landslides* 9(2): 205-214, <https://doi.org/10.1007/s10346-011->
473 0293-5.
- 474 Chen, Z.Y. 2001. A three-dimensional limit equilibrium method for slope stability
475 analysis. *Chinese Journal of Geotechnical Engineering* (05): 525-529.
- 476 Cheng, Y.M., Yip, C. J. 2007. Three-Dimensional Asymmetrical Slope Stability
477 Analysis Extension of Bishop's, Janbu's, and Morgenstern-Price's Techniques. *Journal*
478 *of Geotechnical and Geoenvironmental Engineering* 133(12): 1544-1555,
479 [https://doi.org/10.1061/\(asce\)1090-0241\(2007\)133:12\(1544\)](https://doi.org/10.1061/(asce)1090-0241(2007)133:12(1544)).
- 480 Chopra, A.K. 1966. The importance of the vertical component of earthquake motions.
481 *Bulletin of the Seismological Society of America* 56(5): 1163-1175.
- 482 Conte, E., Troncone, A. 2017. A simplified method for predicting rainfall-induced
483 mobility of active landslides. *Landslides*. 14(1): 35-45, <https://doi.org/10.1007/s10346->
484 016-0692-8.
- 485 David, K.K. 2000. Statistical analysis of an earthquake-induced landslide distribution-
486 the 1989 Loma Prieta, California event. *Engineering Geology* 58(3-4): 231-249,
487 [https://doi.org/10.1016/s0013-7952\(00\)00037-5](https://doi.org/10.1016/s0013-7952(00)00037-5).
- 488 Farzaneh, O., Askari, F., Ganjian, N. 2008. Three-Dimensional Stability Analysis of
489 Convex Slopes in Plan View. *Journal of Geotechnical and Geoenvironmental*
490 *Engineering* 134(8): 1192-1200, [https://doi.org/10.1061/\(asce\)1090-](https://doi.org/10.1061/(asce)1090-)
491 0241(2008)134:8(1192).



-
- 492 Griffiths, D.V., Lane, P. A. 1999. Slope stability analysis by finite elements.
493 *Geotechnique* 49 (3): 387-403.
- 494 Guo, M.W., Ge, X.R., Wang, S.L., Wang, H. 2011. Dynamic stability analysis of slope
495 based on vector sum analysis method. *Chinese Journal of Rock Mechanics and*
496 *Engineering* 30(3): 572-579.
- 497 Hoek, E., Bray, J.W., 1977. *Rock Slope Engineering*. The Institute of Mining and
498 Metallurgy, London.
- 499 Hungr, O. 1987. An extension of Bishop's simplified method of slope stability analysis
500 to three dimensions. *Geotechnique* 37(1): 113-117,
501 <https://doi.org/10.1680/geot.1987.37.1.113>.
- 502 Ishii, Y., Ota, K., Kuraoka, S., Tsunaki, R. 2012. Evaluation of slope stability by finite
503 element method using observed displacement of landslide. *Landslides* 9(3), 335-348,
504 <https://doi.org/10.1007/s10346-011-0303-7>.
- 505 Iverson, R.M. 2000. Landslide triggering by rain infiltration. *Water Resources Research*
506 36(7): 1897-1910, <https://doi.org/10.1029/2000WR900090>.
- 507 Jibson, R.W., Harp, E.L. 2016. Ground Motions at the Outermost Limits of Seismically
508 Triggered Landslides. *Bulletin of the Seismological Society of America* 106(2): 708-
509 719, <https://doi.org/10.1785/0120150141>.
- 510 Lew, M. 1991. Characteristics of Vertical Ground Motions Recorded During the Lorna
511 Prieta Earthquake. *Geotechnique* 41(1): 35-39.
- 512 Ling, H.I., Mohri, Y., Kawabata, T. 1999. Seismic analysis of sliding wedge: extended



-
- 513 Francais-Culmann's analysis. *Soil Dynamics and Earthquake Engineering* 18(5): 387-
514 393, [https://doi.org/10.1016/s0267-7261\(99\)00005-6](https://doi.org/10.1016/s0267-7261(99)00005-6).
- 515 Liu, L. P., Lei, Z.Y., Zhou, F.C. 2001. The evaluation of seismic slope stability analysis
516 methods. *Journal of Chongqing Jiaotong University* 20(3): 83-88.
- 517 Marc, O., Meunier, P., Hovius, N. 2017. Prediction of the area affected by earthquake-
518 induced landsliding based on seismological parameters. *Natural Hazards and Earth*
519 *System Sciences* 17(7): 1159-1175, <https://doi.org/10.5194/nhess-17-1159-2017>.
- 520 Michalowski, R.L. 1995. Slope stability analysis: a kinematical approach.
521 *Geotechnique* 45 (2): 283-293.
- 522 Morgenstern, N.R., Price, V. E. 1965. The analysis of the stability of general slip
523 surfaces. *Geotechnique* 15: 79-93, <https://doi.org/10.1680/geot.1965.15.1.79>.
- 524 Qin, C.B., Chian, S.C. 2018. Kinematic analysis of seismic slope stability with a
525 discretisation technique and pseudo-dynamic approach: a new perspective.
526 *Geotechnique* 68 (6): 492-503.
- 527 Rahardjo, H., Nio, A.S., Leong, E.C., Song, N.Y. 2010. Effects of Groundwater Table
528 Position and Soil Properties on Stability of Slope during Rainfall. *Journal of*
529 *Geotechnical and Geoenvironmental Engineering* 136(11): 1555-1564,
530 [https://doi.org/10.1061/\(asce\)gt.1943-5606.0000385](https://doi.org/10.1061/(asce)gt.1943-5606.0000385).
- 531 Salinas-Jasso, J.A., Ramos-Zuniga, L.G., Montalvo-Arrieta, J.C. 2019. Regional
532 landslide hazard assessment from seismically induced displacements in Monterrey
533 Metropolitan area, Northeastern Mexico. *Bulletin of Engineering Geology and the*



-
- 534 Environment 78(2): 1127-1141, <https://doi.org/10.1007/s10064-017-1087-3>.
- 535 Sassa, K., Nagai, O., Solidum, R., Yamazaki, Y., Ohta, H. 2010. An integrated model
536 simulating the initiation and motion of earthquake and rain induced rapid landslides
537 and its application to the 2006 Leyte landslide. Landslides 7(3): 219-236,
538 <https://doi.org/10.1007/s10346-010-0230-z>.
- 539 Sepúlveda, S. A., Murphy, W., Jibson, R.W., Petley, D.N. 2005. Seismically induced
540 rock slope failures resulting from topographic amplification of strong ground motions:
541 The case of Pacoima Canyon, California. Engineering Geology 80(3-4): 336-348,
542 <https://doi.org/10.1016/j.enggeo.2005.07.004>.
- 543 Shukha, R., Baker, R. 2008. Design implications of the vertical pseudostatic coefficient
544 in slope analysis. Computers and Geotechnics 35(1): 86-96,
545 <https://doi.org/10.1016/j.compgeo.2007.01.005>.
- 546 Spencer, E. 1967. A method of analysis of the stability of embankments assuming
547 parallel inter-slice forces. Geotechnique 17: 11-26. doi:10.1680/geot.1967.17.1.11.
- 548 Sun, G.H., Cheng, S.G., Jiang, W., Zheng, H. 2016. A global procedure for stability
549 analysis of slopes based on the morgenstern-price assumption and its applications.
550 Computers and Geotechnics 80(dec.): 97-106,
551 <https://doi.org/10.1016/j.compgeo.2016.06.014>.
- 552 Sun, G.H., Yang, Y.T., Jiang, W., Zheng, H. 2017. Effects of an increase in reservoir
553 drawdown rate on bank slope stability: a case study at the three gorges reservoir, China.
554 Engineering Geology 221: 61-69, <https://doi.org/10.1016/j.enggeo.2017.02.018>.



-
- 555 Wang, H.L., Xu, W.Y. 2005. 3D dynamical response analysis of high rock slope related
556 to hydropower project in high intensive seismic region. Chinese Journal of Rock
557 Mechanics and Engineering 24(2): 5890-5895.
- 558 Zhang, X. 1988. Three-dimensional stability analysis of concave slopes in plan view.
559 Journal of Geotechnical and Geoenvironmental Engineering 114(6): 658-671.
560 [https://doi.org/10.1061/\(asce\)0733-9410\(1988\)114:6\(658\)](https://doi.org/10.1061/(asce)0733-9410(1988)114:6(658)).
- 561 Zheng, H. 2007. A rigorous three-dimensional limit equilibrium method. Chinese
562 Journal of Rock Mechanics and Engineering 26(8): 1529-1537.
563 <https://doi.org/10.3321/j.issn:1000-6915.2007.08.002>.
- 564 Zheng, H. 2009. Eigenvalue problem from the stability analysis of slopes. Journal of
565 Geotechnical and Geoenvironmental Engineering 135(5): 647-656,
566 [https://doi.org/10.1061/\(asce\)gt.1943-5606.0000071](https://doi.org/10.1061/(asce)gt.1943-5606.0000071).
- 567 Zheng, Y. R., Shi, W. M., Kong, W.X. 2004. Calculation on seepage forces and phreatic
568 surface under drawdown condition. Chinese Journal of Rock Mechanics and
569 Engineering 23(18): 3203-3210, <https://doi.org/10.16285/j.rsm.2018.1617>.
- 570 Zhou, J. F., Qin, C.B. 2022. Stability analysis of unsaturated soil slopes under reservoir
571 drawdown and rainfall conditions: steady and transient state analysis. Computers and
572 Geotechnics 142: 104541-, <https://doi.org/10.1016/j.compgeo.2021.104541>.
- 573 Zhou, J., Chen, Q., Wang, J. 2017. Rigid block based lower bound limit analysis method
574 for stability analysis of fractured rock mass considering rock bridge effects. Computers
575 and Geotechnics 86: 173-180.